Dispersion of the nonlinear susceptibility of MoS₂ and WS₂ from second-harmonic scattering spectroscopy

Dispersion of the nonlinear susceptibility of MoS_2 and WS_2 from second-harmonic scattering spectroscopy

Kévin Bredillet,[1] Jérémy Riporto,[1,2] Gregory T. Forcherio [ORCID],[3] Jeremy R. Dunklin,[4] Jean-Pierre Wolf [ORCID],[2] Luigi Bonacina [ORCID],[2] Yannick Mugnier [ORCID],[1] and Ronan Le Dantec [ORCID][1,*]

[1]*Univ. Savoie Mont Blanc, SYMME, F-74000 Annecy, France*
[2]*Department of Applied Physics-GAP, Université de Genève, 22 Chemin de Pinchat, CH-1211 Geneva, Switzerland*
[3]*Electro-Optic Technology Division, Naval Surface Warfare Center, Crane, Indiana 47522, USA*
[4]*Chemistry and Nanoscience Center, National Renewable Energy Laboratory, Golden, Colorado 80401, USA*

Dispersion of the absolute second-order susceptibility of both MoS_2 and WS_2 is assessed on a wide spectral excitation range (710–1300 nm) by using second-harmonic scattering spectroscopy (SHS). SHS is an accurate ensemble measurement here applied on well-dispersed suspensions of monodisperse liquid-exfoliated nanosheets showing a high monolayer content. The as-derived, high susceptibility values shed light on the discrepancies between available literature values while evidencing resonances associated with the main excitonic transitions.

I. INTRODUCTION

Nonlinear optical properties of two-dimensional (2D) layered materials are the subject of extensive research [1]. Among 2D materials, transition metal dichalcogenides (TMDs) constitute an attractive class because their lack of inversion symmetry confers them a strong second-order nonlinear optical response [2]. Early studies [3,4] reported very high values of the quadratic susceptibility $\chi^{(2)}$, on the order of 10^2 pm/V, then leading to a significant amount of work in this area. One of the important features of TMDs is the relationship between second-harmonic generation (SHG) and the number of layers. It was demonstrated that SHG is only observed with an odd number of layers [3,4]. For even numbers, coherent superposition of the opposite second-harmonic (SH) fields generated within each layer results in cancellation of the signal at 2ω. The relationship between the stacking structure and SHG has since been exploited as a tool for TMD characterizations, to probe for instance their crystalline orientation [3] and to study homo- and heterostructured multilayer structures [5]. Another notable property of TMDs stems from the strong excitonic resonances observed in 2D materials resulting in significant enhancement of the SHG emissions around the transitions [6].

Interestingly, the MoS_2 quadratic susceptibility at discrete excitation wavelengths has already been estimated (Supplemental Table S1 [7]), but a large discrepancy can be found in the literature with $\chi^{(2)}$ values spanning three orders of magnitude [1]. This large discrepancy is probably due to the difficulty in measuring and modeling the SHG response from 2D monolayers. SHG microscopy is a commonly used technique to analyze the SH signal emitted by single layers, but deriving accurate quantitative values is a challenging task since the absolute calibration of a SHG microscope requires careful procedures, especially on a large spectral range. The best approach is likely to compare signals coming from monolayers and a reference material, e.g., a quartz crystal, treating individual nanosheets as a nonlinear polarization sheet. However, a different model making use of a standard SHG reflection formalism is typically employed for the reference crystal [4,8,9], and most studies do not consider deviations that could occur under tight optical focusing conditions with high numerical-aperture (NA) objectives. On the other hand, a direct calibration using an estimated incident intensity at the beam waist was also proposed to derive the TMD susceptibility [10–12], but this approach appears to be delicate due to very precise identification of all beam parameters that must be integrated. The effect of the substrate can also strongly modify the emitted SH signal due to additional interference contributions [12,13], and strain artifacts are known to result in SHG variations [14]. In terms of TMD materials, a few studies have highlighted the effect of crystalline quality on discrepancies between the published $\chi^{(2)}$ values between mechanically exfoliated samples and those obtained from chemical vapor deposition (CVD) [10,15]. Regarding WS_2, less work has been performed [9,12,16,17], but similar observations have been noted.

There exists significant interest in measuring SHG behavior of 2D TMDs with new characterization methods, associated with appropriate models, to address these knowledge gaps. Determination of the $\chi^{(2)}$ dispersion is also very fundamentally relevant in order to quantitatively study the resonances associated with the different optoelectronic transitions. The first study by Malard *et al.* [3] showed a significant amplification of the SHG around the C exciton within MoS_2 layers. Several reports have since confirmed that an enhancement occurs around the three main UV-visible excitonic

*ronan.le-dantec@univ-smb.fr

transitions, typically denoted as A, B, and C [6,18,19]. One can also expect that quantitative dispersion measurements will lead to a better understanding of the nonlinear optical properties of TDMs through comparison with theoretical models [20,21].

In this paper, we use second-harmonic scattering (SHS) spectroscopy to quantitatively assess the absolute, orientation-averaged second-order susceptibility of both MoS_2 and WS_2. SHS spectroscopy is an ensemble measurement probing under low focusing conditions a very large number of sheets within TMD suspensions. This alternative approach was initially employed to derive the susceptibility of WS_2 at a single excitation wavelength of 1064 nm [22]. This work expands scope to a wide excitation range (710–1300 nm) via a femtosecond tunable laser source to assess dispersion of the orientation-averaged $\chi^{(2)}$ and to probe impacts of the excitonic resonances of MoS_2 and WS_2 on their $\chi^{(2)}$ dispersion magnitude. Consistency and suitability of the SHS technique are demonstrated from different liquid-exfoliated TMD suspensions consisting of freestanding, dispersed nanosheets with typical lateral dimension below 100 nm and a high proportion of monolayers (42–75%).

II. EXPERIMENTAL PROCEDURES

Monolayer to few-layer nanosheets of WS_2 and MoS_2 were suspended in aqueous solutions via liquid-phase exfoliation (LPE) [23] followed by a liquid-cascade centrifugation process [24], which together offers low-cost, scalable production of low-dimensional TMDs for SHS spectroscopy. Briefly, bulk WS_2 and MoS_2 powders (Sigma-Aldrich) were dispersed at a concentration of 25 mg/mL into an aqueous sodium cholate surfactant solution (6 mg/mL, 80 mL total volume) and probe sonicated at 360 W (600 W Cole-Parmer; 60% amplitude) immersed in an ice-water bath. After an initial purification and cleaning step [24], the TMD powder dispersions were sonicated for 7 h with a 5-h on-, 2-h off-cycle for exfoliation. Size separation of the exfoliated nanosheet dispersions was executed via a liquid-cascade centrifugation process previously described [24]. Generally, nanosheets trapped at higher centrifugation speeds are smaller in both thickness and lateral dimensions. Monolayer-rich WS_2 and MoS_2 dispersions used in this paper were trapped between 10 and 18 krpm (7.5 and 24.4 k*g*) and between 14 and 24 krpm (14.8 and 43.4 k*g*), respectively (Supplemental Fig. S1). Suspensions of the monolayer-rich TMD dispersions stabilized with sodium cholate are thus obtained with no observable aggregation.

Mean nanosheet layer quantity, lateral size, and monolayer concentration metrics for each WS_2 and MoS_2 dispersion were assessed by empirical relationships derived from transmission UV-visible metrics, as detailed extensively in Refs. [24,25]. Representative absorbance spectra for WS_2 and MoS_2 are shown in Fig. 1, which contain size- and thickness-dependent signatures due to electronic structure and quantum confinement effects at the nanosheet edges. Such quantitative correlation between the intensity- and wavelength-occurrence of various spectroscopy absorbance features to size metrics of these TMD dispersions at less than 10% uncertainty has been intensely explored via statistical atomic force and transmission electron microscopies (AFM and TEM, respectively)
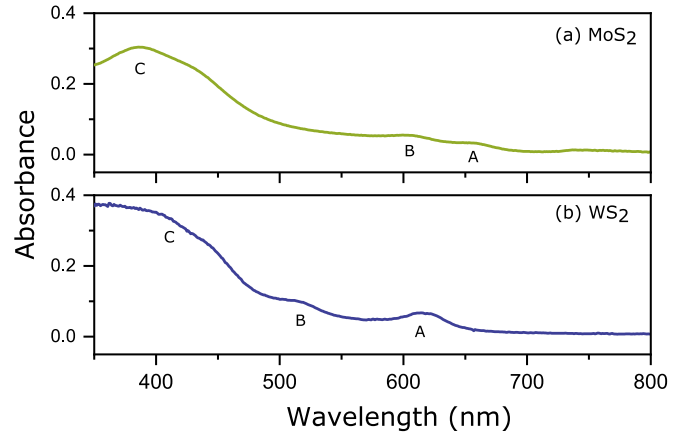

FIG. 1. Absorbance spectra of the (a) MoS_2 and (b) WS_2 suspensions (sample w3 for WS_2; see Table I). The A, B, and C excitonic transitions are labeled.

[24–26] and dynamic light scattering (DLS) [27]. The procedure has been applied in the study of numerous 2D material systems [28–33]. Here, three different WS_2 suspensions and one MoS_2 suspension were prepared for optical characterization with measured metrics summarized in Table I.

Our approach for the measurement of the orientation-averaged second-order susceptibility is fully described in a recent publication [34], where the susceptibility dispersion of several nanomaterials such as $LiNbO_3$ (LN), $BiFeO_3$, and ZnO is quantitatively assessed in the 700–1300-nm excitation range. A two-step procedure is applied. Dispersion of the relative susceptibility is first determined by measuring for each wavelength the SH intensity scattered by a suspension before applying a protocol for correcting the spectral response of the setup. The absolute value of the susceptibility is then retrieved at 1064 nm by comparison with the well-known hyperpolarizability of *para*-nitroaniline (pNA) molecules dissolved in methanol [35].

Briefly, the intensity of the SH signal scattered from a colloidal suspension without any solvent contribution can be expressed as

$$I_{2\omega} = GNT\langle\beta^2\rangle I_\omega^2. \qquad (1)$$

G is an experimental parameter, and N is the number concentration of nonlinear emitters, namely, nanosheets here. T is a field factor which connects the incident electric field to the

TABLE I. Sample parameters and measured susceptibilities at 1064-nm excitation. $\langle N \rangle$, mean layer quantity; mVf, monolayer volume fraction; $\langle L \rangle$, mean length; $\langle \beta \rangle$, orientation-averaged hyperpolarizability; $\chi^{(2)}_{xxx}$, bulk susceptibility.

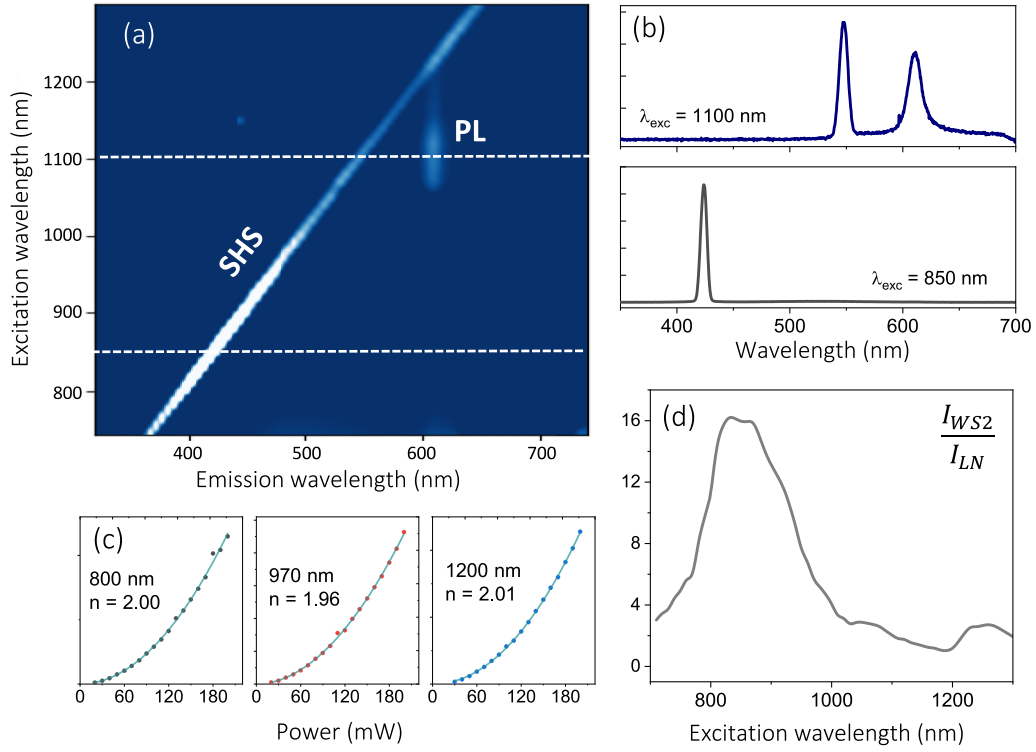| Sample code | WS2 | | | MoS2 |
	w1	w2	w3	
$\langle N \rangle$	1.7	1.7	1.1	1.5
mVf (%)	42	50	75	51
$\langle L \rangle$ (nm)	42	30	25	80
$\langle \beta \rangle$ (10^{-26} esu)	15.8	5.9	8.0	20.1
$\chi^{(2)}_{xxx}$ (pm/V)	370 ± 50	270 ± 110	530 ± 210	130 ± 50

FIG. 2. (a) Surface map of scattering intensity at a given wavelength (x axis) as a function of the excitation wavelength (y axis, 10-nm wavelength increments) for a WS_2 suspension (sample w2; see Table I). (b) Specific spectra at 850 and 1100 nm extracted from (a) showing pure SHG and both SHG and two-photon photoluminescence (PL), respectively. (c) Power dependence of SH signal at 800-, 970-, and 1200-nm excitation. The value of n power resulting from the fit of the experimental curves with $A I_\omega^n$ is shown. (d) Experimental ratio of the SHS intensity I_{WS_2} and I_{LN} from WS_2 and LN suspensions, respectively, according to the excitation wavelength.

inner macroscopic field within nanoparticles (see Supplemental Material [7]). For spherical nanoparticles, T is calculated from the quasistatic approximation provided for a sphere, which allows us to estimate the inner field according to the refractive indices of the solvent and of the particles [36]. However, this approximation is no longer appropriate for a 2D nanosheet, and we here assume, because of the ultrathin monolayer thickness, that the incident fundamental field is not modified within the nanosheet, i.e., $T = 1$ [22]. Importantly, this assumption is the same as the one commonly used to describe a nonlinear polarization sheet deposited on top of a substrate. The fundamental electric field at the substrate surface is presumably not modified by the presence of a monolayer [37].

Finally, $\langle\beta^2\rangle^{\frac{1}{2}} = \langle\beta\rangle$ is the effective hyperpolarizability averaged over all possible orientations. This experimental parameter is simply related to the sheet susceptibility $\langle\chi_s^{(2)}\rangle$ as

$$\langle\chi_s^{(2)}\rangle = \frac{2\langle\beta\rangle}{S}, \qquad (2)$$

with S being the sheet surface. Dividing this sheet susceptibility by the monolayer thickness ($t = 0.65$ nm) then allows derivation of the effective volume susceptibility $\langle\chi^{(2)}\rangle$ as usually reported in previous works. Comparison with the single nonzero tensor element $\chi_{xxx}^{(2)}$ retrieved in typical SHG microscopy experiments is then readily achieved since the orientation-averaging procedure leads to $\chi_{xxx}^{(2)} = -\chi_{xyy}^{(2)} =$

$-\chi_{yyx}^{(2)} = \chi_{yxy}^{(2)} = (21/8)^{1/2}\langle\chi^2\rangle$ for the D_{3h} point-group symmetry of TMD monolayers [22].

The experimental setup described in Ref. [34] is based on a femtosecond laser (Spectra Physics Insight X3) with a wide wavelength tuning range (680–1300 nm). The incident beam power is controlled and kept constant over the full excitation range after careful calibration of a half-wave plate (FR600HM; Thorlabs) associated with a vertical Glan-Thomson polarizer. An achromatic lens (Newport, $f = 30$ mm) is here used to focus the incident beam into a microcuvette (CV10Q700FS; Thorlabs) containing the TMD nanosheet suspension. The optical excitation path here restrained to the 2 mm of the cuvette thickness allows us to limit self-defocusing that may arise for an incident beam power above 200 mW. The SH signal collected perpendicularly to the incident beam is then focused through two fused silica lenses ($f = 50$ mm) into the entrance slit of a spectrometer (Andor Shamrock 193) coupled to a CCD camera (Andor iDus 401). According to the excitation wavelength, a low-pass filter (FESH0700 or FGB37; Thorlabs) is placed in front of the spectrometer to remove any scattered signal from the fundamental beam.

III. EXPERIMENTAL RESULTS AND DISCUSSION

The relative susceptibility measurements performed on WS_2 are summarized in Fig. 2, including emission spectra [Figs. 2(a) and 2(b)], power-dependence plots [Fig. 2(c)],

and magnitude ratio of WS_2 SHS normalized to that of LN [Fig. 2(d)]. The measured emission spectra consistently feature a SH signal at 2ω, while a subset ($\sim$1050–1200-nm excitation range) additionally displays a two-photon excited photoluminescence signal associated with the A exciton transition. This is illustrated verbatim in Fig. 2(b). The SHS intensity from each emission spectrum was estimated using a Gaussian fitting procedure and normalized using the SHS intensity collected from a LN suspension. Indeed, raw SHS intensity values are obviously related to the spectral response of each optical element comprising the instrumentation setup. LN suspension can be considered as an ideal reference for the calibration route since LN has a known susceptibility $\langle \chi^{(2)} \rangle^{LN}$ which moreover slightly varies over the studied wavelength range [34]. The resulting SHS intensity ratio I_{WS_2}/I_{LN}, shown in Fig. 2(d), represents the instrumentation-corrected SHS signal from which the relative susceptibility is calculated as [34]

$$\langle \chi^{(2)} \rangle^{WS_2}_{Rel} \propto \left(\frac{I_{WS_2}}{I_{LN}} \, T_{LN} \right)^{\frac{1}{2}} \langle \chi^{(2)} \rangle^{LN}, \tag{3}$$

where T_{LN} is here the field factor calculated for LN nanoparticles. The resulting relative susceptibility for WS_2 is depicted in Supplemental Fig. S2.

As described in our previous work [34], there are some experimental parameters that require specific attention to obtain robust SHS measurements. Firstly, the SHS signal can be reabsorbed if particle suspensions are not transparent at the SH wavelength (i.e., SHS signal either falls within an absorption band of the probed sample or is strongly scattered within the suspension). To avoid this issue, sample must be diluted enough until reabsorption and scattering of the SH are negligible. A linearly proportional relationship between SHS signal and nanosheet number density is then observed, per Eq. (1), which is confirmed in Fig. 3 where number density values are sufficiently low ($< 3 \times 10^{12}$ cm^{-3}). A second potential issue can arise with the possibility of thermal lensing that can cause variations in the excitation intensity I_ω, which should be kept constant across the full excitation range. Herein, the laser power was fixed (100 mW), and an achromatic lens was used to focus the beam such that no change of the focus waist parameters should be observed. Self-defocusing through thermal lensing was noticed, however, at too high incident power exceeding 200 mW and within solvent absorption bands (namely, at $\lambda = 970$ nm and $\lambda = 1200$ nm for water [38]). This can lead to a change in the waist size and position and consequently a variation in the excitation intensity. Here, the absence of self-defocusing is attested from the ideal quadratic behavior observed in Fig. 2(c) for the two most sensitive excitation wavelengths (970 and 1200 nm). After confirming the absence of these two procedural caveats, reproducible SHS intensity values over a wide excitation range were obtained. The ratio I_{WS_2}/I_{LN} in Fig. 2(d) shows the relative intensity of SHS from WS_2 after correcting for instrument function of the setup, where three resonances associated with the excitonic transitions of WS_2 are apparent. They will be discussed in more detail later. The same experimental procedure was then applied to MoS_2 suspensions, whose results are presented in Supplemental Fig. S3. For
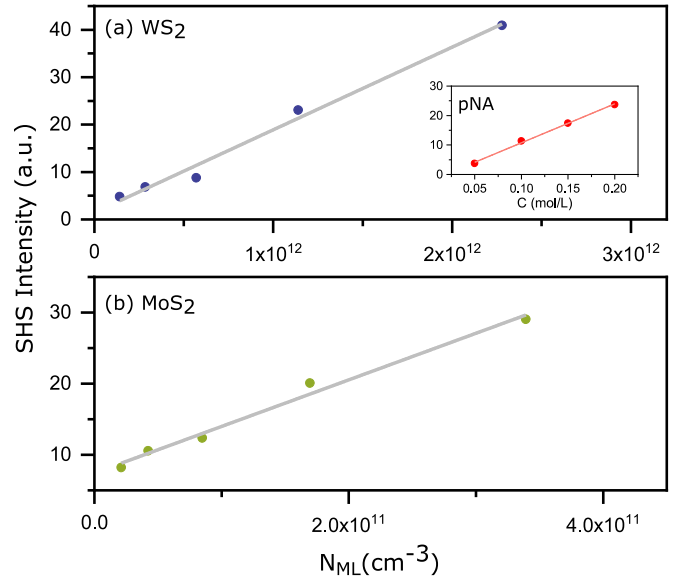

FIG. 3. Concentration-dependent SH signals at $\lambda_{exc} = 1064$ nm for (a) WS_2 (sample w2; see Table I) and pNA and (b) MoS_2. N_{ML} is the number density of monolayers, and C is the molar concentration of pNA in methanol.

each excitation wavelength, emission spectra show a dominant SH signal together with two weak peaks. A background signal also appeared with unknown origin, but persisted across multiple MoS_2 samples at varying concentrations, sizes, and syntheses. In any case, it was straightforward to deconvolve the SHS contribution from these spurious signals such that Supplemental Fig. S3(b) displays the ratio I_{MoS_2}/I_{LN} resulting from these measurements.

Absolute measurements of $\chi^{(2)}$ are then performed at 1064 nm from the linear increase in SH intensities versus TMD (and pNA) concentrations, as described in Ref. [22]. From the measured slopes in Fig. 3, the TMD hyperpolarizability $\langle \beta \rangle$ can be calculated according to the standard formalism detailed in the Supplemental Material [7]. For TMDs, we remind the reader that only an odd number of layers can generate a SH signal and that, in a first-step approximation, odd layers all generate the same SH signal [11]. For each sample of Table I, typical layer distributions [26] show that the fraction of nanosheets with at least three layers is less than 10%. We thus assume that the SH signal from high-order odd layers is negligible and that the relevant number concentration is the monolayer number concentration N_{ML}. This parameter can be calculated from the weight concentration and monolayer volume fraction (mVf; see Supplemental Material [7]). The resulting $\chi^{(2)}$ values for WS_2 and MoS_2 are presented in Table I. For WS_2, the measurements were performed on three independent suspensions with different monolayer volume fractions and size metrics. We obtained high $\chi^{(2)}_{xxx}$ values at 1064 nm varying between 270 and 530 pm/V. For MoS_2, $\chi^{(2)}_{xxx}$ was derived to be 130 pm/V.

The benefit of the above approach is to propose an alternative method to SHG microscopy experiments, which is based here on ensemble measurements as already validated with other nanomaterials [34] and 2D sheets at 800 nm [39]. One major limitation for absolute measurements can be
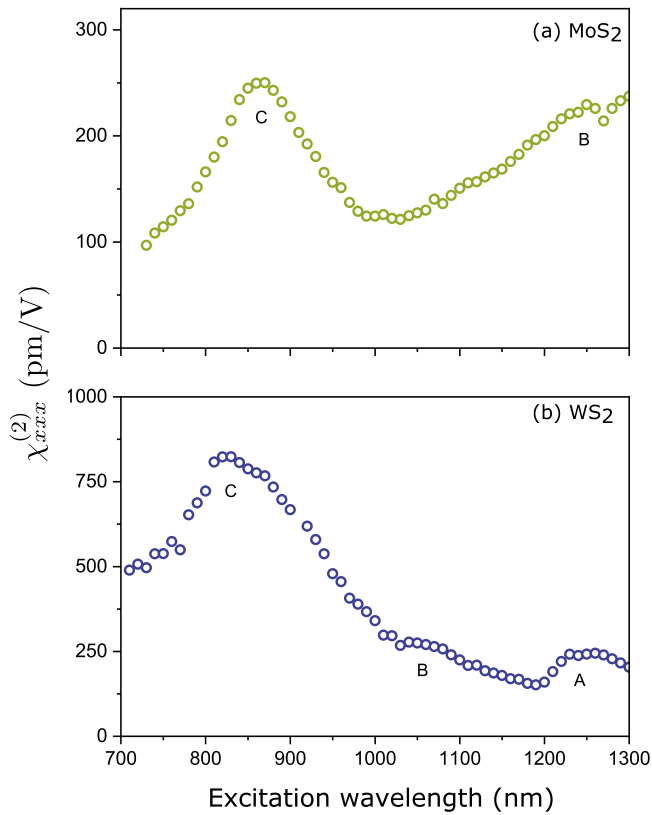
FIG. 4. Absolute nonlinear susceptibility $\chi^{(2)}_{xxx}$ of (a) MoS$_2$ and (b) WS$_2$ (sample w2; see Table I).

related, though, to the dispersion of the sample characteristics (nanosheet dimensions, distribution of the layer number), which is the reason why we used several suspensions of known metrics and with the highest possible monolayer content. The main uncertainty originates from the surface area estimation. According to TEM images, a rectangular shape with an average aspect ratio of 2 (i.e., $\langle S \rangle = \langle L \rangle^2 /2$) is usually retained [25]. Although uncertainty in L results in negligible change in the calculated susceptibility [22], deviations in ideal rectangular shape at the same L result in uncertainties of ca. $\pm 40\%$ in the calculated susceptibilities when the aspect ratio is arbitrarily changed from 1 to 4 while keeping L constant. If consistent $\chi^{(2)}$ values are thus obtained in Table I between the three different WS$_2$ samples, we point out that only a further reduction in the nanosheet polydispersity can result at this stage in better quantitative assessments.

Finally, both relative measurements and absolute data at 1064 nm were combined to calculate the dispersion of the absolute $\chi^{(2)}$ over the excitation range as illustrated in Fig. 4. As previously discussed, our protocol allows us to account for the setup spectral response with high precision and reproducibility. We have, moreover, investigated the possible influence of the monolayer volume fraction on the spectral response of $\chi^{(2)}$. In Supplemental Fig. S2, the relative measures found for WS$_2$ samples w2 and w3 are very similar; only a slightly higher resonance at 830 nm is observed for sample w3 with the highest proportion of monolayers. The absence of any wavelength shift [19] is to be mentioned, suggesting that the SH response within suspensions mainly originates from

monolayers. However, we cannot exclude a contribution of the flake edges to the measured composite $\chi^{(2)}$ susceptibility for these nanosheets with low lateral dimensions. It was demonstrated that the SHG response could be modulated by the edge-type termination of the nanosheets, resulting in appearance of a resonance near 1300-nm excitation wavelength and higher overall magnitude [40,41]. The spectral responses shown in Fig. 4 are thus representative of TMD monolayers but may deviate from those typically obtained in SHG microscopy from large flakes obtained by CVD.

The as-derived $\chi^{(2)}$ dispersions for WS$_2$ and MoS$_2$ reveal resonances corresponding to the A, B, and C excitonic transitions in their respective electronic band structures. For MoS$_2$, our data show susceptibility values at about 250 pm/V near the main C excitonic resonance at $\lambda_{exc} \sim 870$ nm, corresponding well with the high-energy shoulder of the C transition resonance at ~ 430 nm [see Fig. 1(a)]. For WS$_2$, we found a generally higher susceptibility than for MoS$_2$ with $\chi^{(2)} \sim 820$ pm/V around the C transition at $\lambda_{exc} \sim 830$ nm. In the linear regime, the C transition arises from a van Hove singularity where bands are parallel between the "Γ" and "Λ" points (commonly called the "nesting" region [42,43]), which provides a large density of states likely responsible for the measurably high $\chi^{(2)}$ magnitude in this region. In the 1000–1300-nm excitation range, our measurements evidence $\chi^{(2)}$ correlation with direct transitions across the "K" point of the Brillouin zone. These are referred to as the A and B excitonic transitions for 2D TMDs in the linear regime but differ in energy due to spin-split valence bands. Both the two-photon A and B "features" were observable for WS$_2$ (at ~ 1230 and ~ 1050 nm, respectively), but excitation of the MoS$_2$ A feature was beyond the excitation capabilities of this setup (occurring beyond 1300 nm).

One interest of this study is to measure on the same experimental setup and over a wide wavelength range the susceptibility of the two most studied TMD materials, MoS$_2$ and WS$_2$, for a direct comparison with literature values. Available data showing the dispersion of the $\chi^{(2)}$ have been normalized and plotted together in Supplemental Fig. S4. These data evidence a strong C exciton resonance in general agreement with our measurements. Comparison with discrete absolute literature values (Supplemental Table S1 and Supplemental Fig. S5) is more problematic due to their large discrepancy, as already introduced. For MoS$_2$, our data are in good agreement with pioneer works [3,4] and a very recent work [9] demonstrating susceptibility values at about several hundreds of pm/V near the main C excitonic resonance. In the 1100–1200-nm excitation range, it should be pointed out that lower values have been measured (30 pm/V near the A transition [8]), whereas susceptibilities at only a few pm/V were obtained under off-resonant conditions at 1560 nm [11,12]. These values clearly contradict our measurements, but we point out that our $\chi^{(2)}$ dispersion spectra allow us to connect the various spectral regions that were separately studied in the literature. If uncertainty of $\pm 40\%$ is here proposed for $\chi^{(2)}$ absolute measurements, our protocol allows us to retrieve the relative dispersion with good accuracy. Our $\chi^{(2)}$ values are significantly higher at the A resonance and probably off-resonance in comparison to those measured in previous studies, possibly attributable to the ostensible contribution of

edge effects as previously discussed. It is, however, difficult to better assess this contribution because of the nanosheet preparation from liquid-cascade centrifugation, which shows a high monolayer concentration but inherently small lateral dimensions. For WS_2, less work has been performed, and a lower susceptibility (275 pm/V) was found in Ref. [9] near the C resonance. In addition, it can be noted that theoretical calculations [20,44] yielded to high values ($\sim$1000 pm/V) for the nonlinear susceptibility of both MoS_2 and WS_2 in this excitation range.

IV. CONCLUSION

Compared with the available literature data, an alternative experimental approach is here used to retrieve in a broader excitation range the $\chi^{(2)}$ dispersion of both MoS_2 and WS_2 nanosheets. From monodisperse and well-characterized liquid-exfoliated TMD suspensions showing a high mono-

layer content and low lateral dimensions, we show that accurate $\chi^{(2)}$ values can be obtained with SHS spectroscopy with uncertainties estimated at $\pm$40% arising from sample polydispersity inherent to both ensemble measurements and liquid exfoliation preparation. $\chi^{(2)}$ dispersion measurements show high susceptibility values over the whole spectral range and clear resonances associated with the main A, B, and C excitonic transitions.

[1] A. Autere, H. Jussila, Y. Dai, Y. Wang, H. Lipsanen, and Z. Sun, Nonlinear optics with 2D layered materials, Adv. Mater. **30**, 1705963 (2018).

[2] Y. Wang, J. Xiao, S. Yang, Y. Wang, and X. Zhang, Second harmonic generation spectroscopy on two-dimensional materials [invited], Opt. Mater. Express **9**, 1136 (2019).

[3] L. M. Malard, T. V. Alencar, A. P. M. Barboza, K. F. Mak, and A. M. de Paula, Observation of intense second harmonic generation from MoS_2 atomic crystals, Phys. Rev. B **87**, 201401(R) (2013).

[4] Y. Li, Y. Rao, K. F. Mak, Y. You, S. Wang, C. R. Dean, and T. F. Heinz, Probing symmetry properties of few-layer MoS_2 and h-BN by optical second-harmonic generation, Nano Lett. **13**, 3329 (2013).

[5] W.-T. Hsu, Z.-A. Zhao, L.-J. Li, C.-H. Chen, M.-H. Chiu, P.-S. Chang, Y.-C. Chou, and W.-H. Chang, Second harmonic generation from artificially stacked transition metal dichalcogenide twisted bilayers, ACS Nano **8**, 2951 (2014).

[6] M. L. Trolle, Y.-C. Tsao, K. Pedersen, and T. G. Pedersen, Observation of excitonic resonances in the second harmonic spectrum of MoS_2, Phys. Rev. B **92**, 161409(R) (2015).

[7] See Supplemental Material at http://link.aps.org/supplemental/10.1103/PhysRevB.102.235408 for a description of the sample preparation, the derivation of the absolute susceptibility at 1064 nm, a comparison of the $\chi^{(2)}$ relative dispersion for WS_2 suspensions, the MoS_2 data, and a comparison with the literature data.

[8] D. J. Clark, C. T. Le, V. Senthilkumar, F. Ullah, H.-Y. Cho, Y. Sim, M.-J. Seong, K.-H. Chung, Y. S. Kim, and J. I. Jang, Near bandgap second-order nonlinear optical characteristics of MoS_2 monolayer transferred on transparent substrates, Appl. Phys. Lett. **107**, 131113 (2015).

[9] K. Yao, E. Yanev, H.-J. Chuang, M. R. Rosenberger, X. Xu, T. Darlington, K. M. McCreary, A. T. Hanbicki, K. Watanabe, T. Taniguchi, B. T. Jonker, X. Zhu, D. N. Basov, J. C. Hone, and P. J. Schuck, Continuous wave sum frequency generation and imaging of monolayer and heterobilayer two-dimensional semiconductors, ACS Nano **14**, 708 (2020).

[10] R. I. Woodward, R. T. Murray, C. F. Phelan, R. E. P. de Oliveira, T. H. Runcorn, E. J. R. Kelleher, S. Li, E. C. de Oliveira, G. J. M. Fechine, G. Eda, and C. J. S. de Matos, Characterization of the second- and third-order nonlinear optical susceptibilities of monolayer MoS_2 using multiphoton microscopy, 2D Mater. **4**, 011006 (2016).

[11] A. Säynätjoki, L. Karvonen, H. Rostami, A. Autere, S. Mehravar, A. Lombardo, R. A. Norwood, T. Hasan, N. Peyghambarian, H. Lipsanen, K. Kieu, A. C. Ferrari, M. Polini, and Z. Sun, Ultra-strong nonlinear optical processes and trigonal warping in MoS_2 layers, Nat. Commun. **8**, 893 (2017).

[12] A. Autere, H. Jussila, A. Marini, J. R. M. Saavedra, Y. Dai, A. Säynätjoki, L. Karvonen, H. Yang, B. Amirsolaimani, R. A. Norwood, N. Peyghambarian, H. Lipsanen, K. Kieu, F. J. G. de Abajo, and Z. Sun, Optical harmonic generation in monolayer group-VI transition metal dichalcogenides, Phys. Rev. B **98**, 115426 (2018).

[13] X. Miao, N. Xuan, Q. Liu, W. Wu, H. Liu, Z. Sun, and M. Ji, Optimizing nonlinear optical visibility of two-dimensional materials, ACS Appl. Mater. Interfaces **9**, 34448 (2017).

[14] J. Liang, J. Zhang, Z. Li, H. Hong, J. Wang, Z. Zhang, X. Zhou, R. Qiao, J. Xu, P. Gao, Z. Liu, Z. Liu, Z. Sun, S. Meng, K. Liu, and D. Yu, Monitoring local strain vector in atomic-layered $MoSe_2$ by second-harmonic generation, Nano Lett. **17**, 7539 (2017).

[15] H. Li, J. Wu, Z. Yin, and H. Zhang, Preparation and applications of mechanically exfoliated single-layer and multilayer MoS_2 and WSe_2 nanosheets, Acc. Chem. Res. **47**, 1067 (2014).

[16] C. Janisch, Y. Wang, D. Ma, N. Mehta, A. L. Elías, N. Perea-López, M. Terrones, V. Crespi, and Z. Liu, Extraordinary second harmonic generation in tungsten disulfide monolayers, Sci. Rep. **4**, 5530 (2014).

[17] M. Mokim, A. Card, and F. Ganikhanov, Nonlinear optical susceptibility of atomically thin WX_2 crystals, Opt. Mater. (Amsterdam, Neth.) **88**, 30 (2019).

[18] D. J. Clark, V. Senthilkumar, C. T. Le, D. L. Weerawarne, B. Shim, J. I. Jang, J. H. Shim, J. Cho, Y. Sim, M.-J. Seong, S. H. Rhim, A. J. Freeman, K.-H. Chung, and Y. S. Kim, Strong

optical nonlinearity of CVD-grown MoS_2 monolayer as probed by wavelength-dependent second-harmonic generation, Phys. Rev. B **90**, 121409(R) (2014).

[19] Y. Kikuchi, Y. Miyauchi, R. Takaoka, T. Suzuki, M. Tanaka, and S. Ohno, Multiple-peak resonance of optical second harmonic generation arising from band nesting in monolayer transition metal dichalcogenides TX_2 on $SiO_2/Si(001)$ substrates ($T =$ Mo, W; $X =$ S, Se), Phys. Rev. B **100**, 075301 (2019).

[20] G. F. Mkrtchian, A. Knorr, and M. Selig, Theory of second-order excitonic nonlinearities in transition metal dichalcogenides, Phys. Rev. B **100**, 125401 (2019).

[21] M. C. Lucking, K. Beach, and H. Terrones, Large second harmonic generation in alloyed TMDs and boron nitride nanostructures, Sci. Rep. **8**, 10118 (2018).

[22] G. T. Forcherio, J. Riporto, J. R. Dunklin, Y. Mugnier, R. L. Dantec, L. Bonacina, and D. K. Roper, Nonlinear optical susceptibility of two-dimensional WS_2 measured by hyper Rayleigh scattering, Opt. Lett. **42**, 5018 (2017); **43**, 2400(E) (2018).

[23] J. N. Coleman, M. Lotya, A. O'Neill, S. D. Bergin, P. J. King, U. Khan, K. Young, A. Gaucher, S. De, R. J. Smith, I. V. Shvets, S. K. Arora, G. Stanton, H.-Y. Kim, K. Lee, G. T. Kim, G. S. Duesberg, T. Hallam, J. J. Boland, J. J. Wang *et al.*, Two-dimensional nanosheets produced by liquid exfoliation of layered materials, Science **331**, 568 (2011).

[24] C. Backes, B. M. Szydłowska, A. Harvey, S. Yuan, V. Vega-Mayoral, B. R. Davies, P.-l. Zhao, D. Hanlon, E. J. G. Santos, M. I. Katsnelson, W. J. Blau, C. Gadermaier, and J. N. Coleman, Production of highly monolayer enriched dispersions of liquid-exfoliated nanosheets by liquid cascade centrifugation, ACS Nano **10**, 1589 (2016).

[25] C. Backes, R. J. Smith, N. McEvoy, N. C. Berner, D. McCloskey, H. C. Nerl, A. O'Neill, P. J. King, T. Higgins, D. Hanlon, N. Scheuschner, J. Maultzsch, L. Houben, G. S. Duesberg, J. F. Donegan, V. Nicolosi, and J. N. Coleman, Edge and confinement effects allow in situ measurement of size and thickness of liquid-exfoliated nanosheets, Nat. Commun. **5**, 4576 (2014).

[26] L. Ueberricke, J. N. Coleman, and C. Backes, Robustness of size selection and spectroscopic size, thickness and monolayer metrics of liquid-exfoliated WS_2, Phys. Status Solidi B **254**, 1700443 (2017).

[27] M. Lotya, A. Rakovich, J. F. Donegan, and J. N. Coleman, Measuring the lateral size of liquid-exfoliated nanosheets with dynamic light scattering, Nanotechnology **24**, 265703 (2013).

[28] K. Synnatschke, P. A. Cieslik, A. Harvey, A. Castellanos-Gomez, T. Tian, C.-J. Shih, A. Chernikov, E. J. G. Santos, J. N. Coleman, and C. Backes, Length- and thickness-dependent optical response of liquid-exfoliated transition metal dichalcogenides, Chem. Mater. **31**, 10049 (2019).

[29] C. Backes, D. Campi, B. M. Szydlowska, K. Synnatschke, E. Ojala, F. Rashvand, A. Harvey, A. Griffin, Z. Sofer, N. Marzari, J. N. Coleman, and D. D. O'Regan, Equipartition of energy defines the size–thickness relationship in liquid-exfoliated nanosheets, ACS Nano **13**, 7050 (2019).

[30] J. R. Dunklin, P. Lafargue, T. M. Higgins, G. T. Forcherio, M. Benamara, N. McEvoy, D. K. Roper, J. N. Coleman, Y.

Vaynzof, and C. Backes, Production of monolayer-rich gold-decorated 2H–WS_2 nanosheets by defect engineering, npj 2D Mater. Appl. **1**, 43 (2017).

[31] S. P. Ogilvie, M. J. Large, M. A. O'Mara, P. J. Lynch, C. L. Lee, A. A. K. King, C. Backes, and A. B. Dalton, Size selection of liquid-exfoliated 2D nanosheets, 2D Mater. **6**, 031002 (2019).

[32] A. Harvey, C. Backes, J. B. Boland, X. He, A. Griffin, B. Szydlowska, C. Gabbett, J. F. Donegan, and J. N. Coleman, Non-resonant light scattering in dispersions of 2D nanosheets, Nat. Commun. **9**, 4553 (2018).

[33] A. Griffin, A. Harvey, B. Cunningham, D. Scullion, T. Tian, C.-J. Shih, M. Gruening, J. F. Donegan, E. J. G. Santos, C. Backes, and J. N. Coleman, Spectroscopic size and thickness metrics for liquid-exfoliated h-BN, Chem. Mater. **30**, 1998 (2018).

[34] J. Riporto, M. Urbain, Y. Mugnier, V. Multian, F. Riporto, K. Bredillet, S. Beauquis, C. Galez, V. Monnier, Y. Chevolot, V. Gayvoronsky, L. Bonacina, and R. Le Dantec, Second harmonic spectroscopy of ZnO, $BiFeO_3$ and $LiNbO_3$ nanocrystals, Opt. Mater. Express **9**, 1955 (2019).

[35] F. L. Huyskens, P. L. Huyskens, and A. P. Persoons, Solvent dependence of the first hyperpolarizability of *p*-nitroanilines: Differences between nonspecific dipole–dipole interactions and solute–solvent H-bonds, J. Chem. Phys. **108**, 8161 (1998).

[36] R. Le Dantec, Y. Mugnier, G. Djanta, L. Bonacina, J. Extermann, L. Badie, C. Joulaud, M. Gerrmann, D. Rytz, J. P. Wolf, and C. Galez, Ensemble and individual characterization of the nonlinear optical properties of ZnO and $BaTiO_3$ nanocrystals, J. Phys. Chem. C **115**, 15140 (2011).

[37] Y. R. Shen, Optical second harmonic generation at interfaces, Annu. Rev. Phys. Chem. **40**, 327 (1989).

[38] J. Campo, F. Desmet, W. Wenseleers, and E. Goovaerts, Highly sensitive setup for tunable wavelength hyper-Rayleigh scattering with parallel detection and calibration data for various solvents, Opt. Express **17**, 4587 (2009).

[39] I. Russier-Antoine, H. Fakhouri, S. Basu, F. Bertorelle, P. Dugourd, P.-F. Brevet, P. Velayudhan, S. Thomas, N. Kalarikkal, and R. Antoine, Second harmonic scattering from mass characterized 2D graphene oxide sheets, Chem. Commun. (Cambridge, U. K.) **56**, 3859 (2020).

[40] X. Yin, Z. Ye, D. A. Chenet, Y. Ye, K. O'Brien, J. C. Hone, and X. Zhang, Edge nonlinear optics on a MoS_2 atomic monolayer, Science **344**, 488 (2014).

[41] K.-I. Lin, Y.-H. Ho, S.-B. Liu, J.-J. Ciou, B.-T. Huang, C. Chen, H.-C. Chang, C.-L. Tu, and C.-H. Chen, Atom-dependent edge-enhanced second-harmonic generation on MoS_2 monolayers, Nano Lett. **18**, 793 (2018).

[42] D. Kozawa, R. Kumar, A. Carvalho, K. Kumar Amara, W. Zhao, S. Wang, M. Toh, R. M. Ribeiro, A. H. Castro Neto, K. Matsuda, and G. Eda, Photocarrier relaxation pathway in two-dimensional semiconducting transition metal dichalcogenides, Nat. Commun. **5**, 4543 (2014).

[43] D. Y. Qiu, F. H. da Jornada, and S. G. Louie, Optical Spectrum of MoS_2: Many-Body Effects and Diversity of Exciton States, Phys. Rev. Lett. **111**, 216805 (2013).

[44] M. L. Trolle, G. Seifert, and T. G. Pedersen, Theory of excitonic second-harmonic generation in monolayer MoS_2, Phys. Rev. B **89**, 235410 (2014).